

Eutectic Structure of Sn–Zn Thin Films Formed during Electrodeposition

M. Saitou* and T. Oi

University of the Ryukyus, Department of Mechanical Systems Engineering, 1 Senbaru Nishihara-cho Okinawa, 903-0213, Japan.

*E-mail: saitou@tec.u-ryukyu.ac.jp

Received: 2 November 2020 / Accepted: 21 December 2020 / Published: 31 January 2021

Sn–Zn thin films electrodeposited from solutions in the range 0.18–1.5 of the charged molar ratio Zn/Sn (R) by rectangular pulse voltages over a megahertz frequency range were investigated using scanning electron microscopy coupled with energy dispersive X-ray (SEM-EDX) spectroscopy and X-ray diffraction. The phases of the Sn–Zn thin films were divided into two groups according to R : when $R < 1$, the electrodeposits comprised only the tetragonal crystal structure of the β -Sn phase. When $R \geq 1$, the electrodeposits comprised β -Sn and hexagonal close-packed crystal structure Zn phase, which formed fine eutectic structure patterns. The periodic distance of the eutectic structure patterns was estimated as 0.57 μm using the Fourier transform of the eutectic structure from the SEM images. The Sn–Zn thin films had smooth surfaces grown formed not by islands, but by layer-by-layer growth. The dependence of the Zn content of Sn–Zn thin films on the cathode potential was consistent with the phenomenological theory of electrodeposition. The potential barriers of Sn^{2+} and Zn^{2+} were determined to be 0.86 and 1.12 V, respectively.

Keywords: Sn–Zn thin film; Eutectic structure; Phenomenological theory of electrodeposition; Layer-by-layer growth

1. INTRODUCTION

Electrodeposited Sn–Zn thin films have attracted research interest owing to their excellent solderability [1,2], good ductility [3], and good corrosion resistance [4,5]. The Zn content of Sn–Zn thin films significantly affects their properties. For example, the 20 wt% Sn–Zn thin films offer excellent corrosion protection [6], and Zn content greater than 80 wt% produces the good surface appearances [7]. The control of the Zn content is a key to the fabrication of Sn–Zn thin films.

According to the Sn–Zn phase diagram [8] at room temperature, a stable phase in the range of 0.036–99.6 at% Sn is a eutectic structure comprising the tetragonal crystal structure of β -Sn and hexagonal close-packed (HCP) crystal structure of Zn phase. Sn–Zn alloys prefer phase separation to

alloying. Scanning electron microscopy (SEM) has been extensively employed to observe electrodeposited Sn–Zn thin films. The contrast of SEM images of conductive materials is dependent on the number of secondary electrons, which tend to increase with the atomic number [9]. Hence, the β -Sn and Zn phases formed bright and dark contrast images, as observed by SEM. However, there have been no reports [10,11] in which SEM images of electrodeposited Sn–Zn thin films comprised bright and dark contrasts. Therefore, it is unclear whether electrodeposited Sn–Zn thin films form eutectic structure patterns and nano β -Sn phases approach each other to nano Zn phases each other [12,13]. Furthermore, the effect of the interfaces between the β -Sn and Zn phases on the physical properties of Sn–Zn thin films has not been revealed.

Recently, a phenomenological theory of electrodeposition has been proposed [14,15]. The elemental content of electrodeposits can be described not by thermal equilibrium variables, but by the cathode potential, potential barriers, and resonant frequencies under given elemental compositions of solutions. This study demonstrates that the Zn content dependence of Sn–Zn thin films on the cathode potential is consistent with the theory.

An anomalous elemental content of electrodeposits formed from Sn–Mn aqueous solutions has been reported [16]. The electrodeposits formed from solutions in the range of the charged molar ratio $Mn/Sn < 1.5$ comprised only β -Sn phases. The present study also demonstrates that an anomalous elemental content of electrodeposits, which comprised only β -Sn phases, occurred when the charged molar ratio Zn/Sn in solutions, $R < 1$.

The aim of this study is to demonstrate that when $R < 1$, electrodeposits comprised only the β -Sn phase, whereas $R \geq 1$, they exhibited eutectic structures comprising β -Sn and HCP Zn phases grown by layer-by-layer. The eutectic structure pattern had a periodic distance of 0.57 μm in Sn–Zn thin films, and the dependence of the Zn content on the cathode potential was consistent with the phenomenological theory of electrodeposition.

2. EXPERIMENTAL SETUP

A copper plate of 30×10 mm² and carbon plate of 50×40 mm² were used as the cathode and anode, respectively. One side of the Cu plate was electrically insulated for Sn–Zn electrodeposits to be formed only on the other side. Aqueous solutions containing the following chemical compounds were prepared: SnSO₄ (0.713 mol L⁻¹), ZnSO₄·4H₂O (0.128–1.07 mol L⁻¹) and KNaC₄H₄O₆·4H₂O (0.5 mol L⁻¹). The prepared solutions of $R = 0.18, 0.9, 1.0$ and 1.5 were strained using a membrane filter of pore size 0.1 μm pore-size before electrodeposition.

The cathode and anode were placed parallel to each other in a cell filled with an aqueous solution, which was maintained at 300 K during electrodeposition. A rectangular pulse voltage with 0.4, 0.45, and 0.5 MHz was supplied by a function generator. A 22 Ω metal film resistor was connected in series with the cell to calculate the cathode potential (defined as the voltage across the electric double layer at the cathode).

As the impedance of the electric double layer at the anode was 27 times smaller than that at the cathode, it was ignored. The impedance between the cathode and anode was negligibly small because of the highly concentrated solution. Hence, the cathode potential was calculated by subtracting the amplitude of the rectangle pulse voltage from the measured voltage across the resistor. Figure 1 shows voltage drops across the resistor when the rectangular pulse voltage with an amplitude of 2 V and frequency of 0.4 MHz was applied. The cathode potential was calculated as 1.5 V.

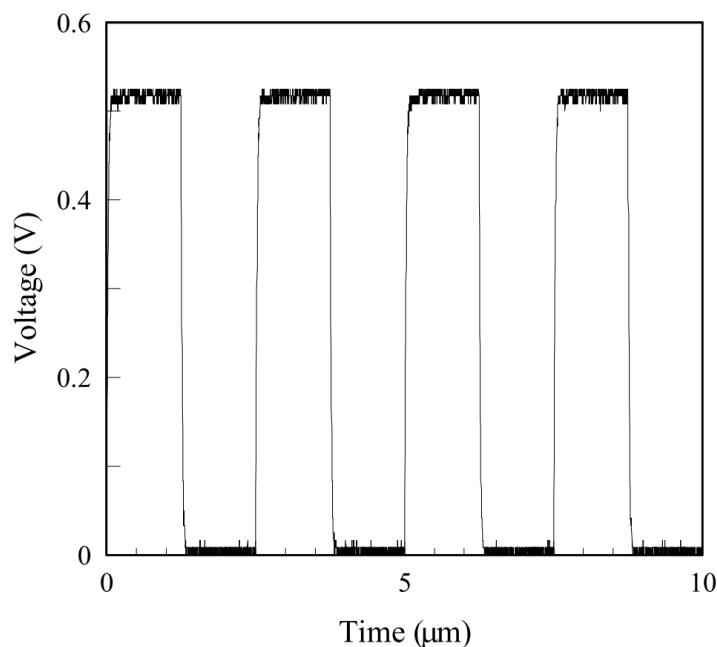


Figure 1. Rectangular pulse voltages measured across the 22 Ω resistor with an amplitude of 2 V and frequency of 0.4 MHz.

After electrodeposition, the Sn–Zn thin films formed on the Cu plate were rinsed with distilled water and dried. The Sn–Zn thin films were weighed to a precision of 0.1 mg with an electric balance to calculate the thickness of the Sn–Zn thin film. Elemental mapping and surface observation of the Sn–Mn thin films were performed using scanning electron microscopy with energy-dispersive X-ray (SEM-EDX) spectroscopy (Hitachi TM3030). Diffractions from the crystallographic planes in the Sn–Zn thin films were investigated using a conventional X-ray diffraction (XRD) (Rigaku Ultima) with CuK α radiation.

3. RESULTS AND DISCUSSION

3.1. Anomalous electrodeposition of Sn–Zn thin films

Figure 2 shows the dependence of the Zn content of Sn–Zn thin films on the cathode potential, V_c . The Sn–Zn thin films were electrodeposited from solutions in a range of $R=0.18$ –1.5 at a frequency of 0.4 MHz.

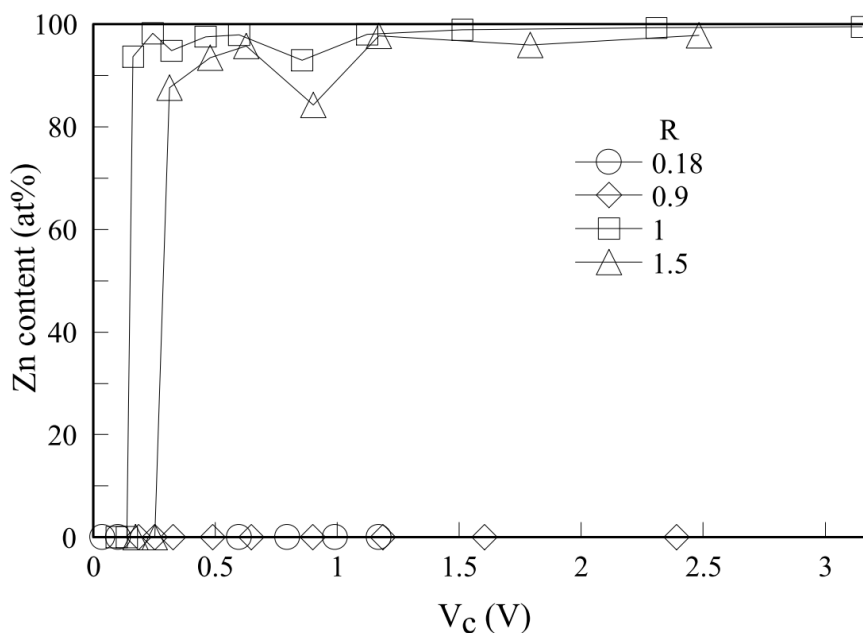


Figure 2. Dependence of the Zn content on V_c . The Sn–Zn thin films were electrodeposited from solutions of $R=0.18, 0.9, 1.0,$ and 1.5 at a frequency of 0.4 MHz.

The Zn content is divided into two regions according to R : When $R < 1$, the electrodeposits do not contain the Zn element irrespective of V_c . This indicates that only the atomization from Sn^{2+} to Sn occurred as if Zn^{2+} ions did not exist near the electric double layer at the Cu plate. The same anomalous electrodeposition in which only Sn element was electrodeposited from a solution containing Sn^{2+} and Mn^{2+} ions was previously reported and explained by the free energy model of the solution [16].

When $R = 1$, the Zn content remains at 0 at% for $V_c \leq 0.14$ V and rapidly increases by 93.7 at% Zn at $V_c = 0.16$ V. This large change within the Zn content occurs in a small range of 0.02 V. The Zn content becomes approximately constant at $V_c \geq 0.16$ V, irrespective of V_c except for $V_c = 0.86$ V. When $R = 1.5$, the Zn content remains at 0 at% for $V_c \leq 0.25$ V and rapidly increases by 87.6 at% at $V_c = 0.31$ V. An obvious decrease in the Zn content occurred at $V_c = 0.9$ V as well as that at $V_c = 0.86$ V, when $R = 1$. The cathode potentials at which the Zn content decreases corresponds to the potential barrier of Sn^{2+} as explained in Section 3.4.

3.2 Eutectic structures of Sn–Zn thin films

Figure 3 shows SEM images of Sn–Zn thin films electrodeposited from solutions of $R = 1$ and 1.5 . The Zn contents of the films shown in Figs. 3 (a) and (b) are 93.6 and 87.6 at%, respectively. The SEM images are composed of bright and dark regions and shows a characteristic of a eutectic structure pattern. These patterns have not been reported in previous studies of electrodeposited Sn–Zn thin films [10–13]. The eutectic structures in Fig. 3 are not parallel platelets (usually called as lamellae, which are often observed in binary eutectic systems), but rather form a labyrinth pattern [17]. In this pattern, a

bright region appears next to a dark region, which is repeated to form periodic structures in its distribution. According to the SEM image contrast theory [9], the secondary electrons from a conductive specimen increases with the atomic number and the number of secondary electrons determines the image contrast. Hence, the bright and dark regions correspond to Sn and Zn phases, respectively.

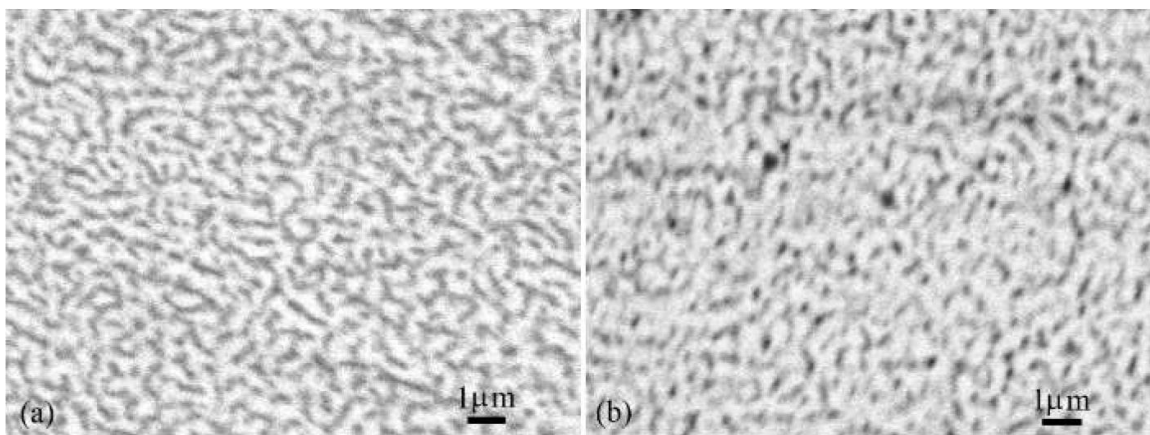


Figure 3. SEM images of Sn–Zn thin films electrodeposited at 0.4 MHz: (a) $R = 1$ and $V_c = 0.16$ and (b) $R = 1.5$ and $V_c = 0.31$ V.

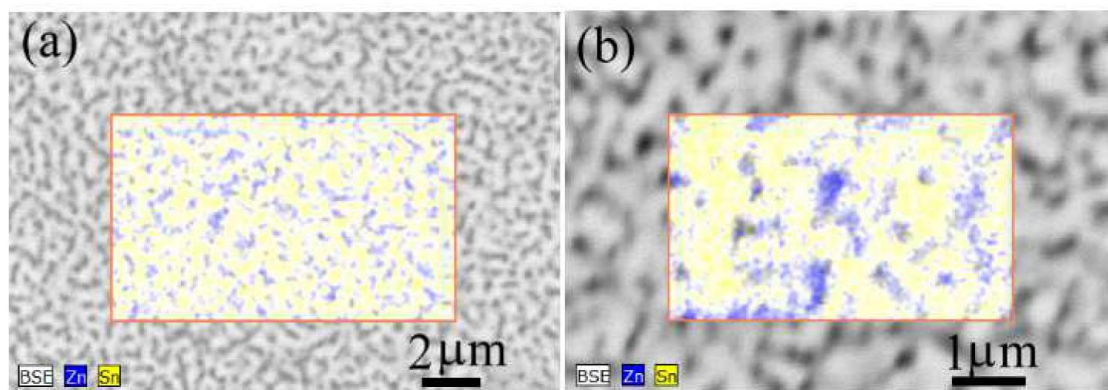


Figure 4. Sn and Zn elemental mapping of the Sn–Zn thin films in Fig. 3.

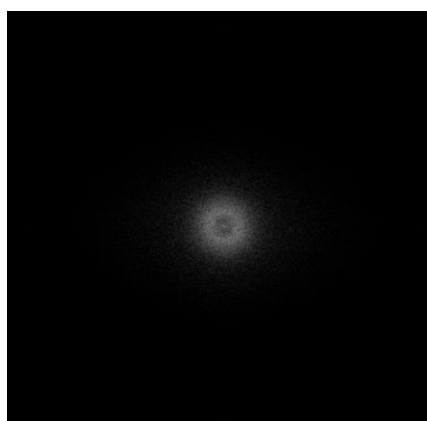


Figure 5. Power spectrum of the SEM image in Fig. 3 (a).

Figure 4 shows the elemental mapping images of the Sn–Zn thin films in Figs. 3 (a) and (b). The yellow and blue regions represent Sn and Zn element, respectively, which are consistent with the bright and dark regions in Fig. 3. The Zn region does not appear to have an island shape, but rather a band shape. This indicates that Sn–Zn thin films were formed by layer-by-layer growth rather than by island growth.

To investigate the periodicity of the Zn band shapes in Fig. 3 (a), a Fourier transformation was performed as shown in Fig. 5. Figure 5 shows the power spectrum of the SEM image in Fig. 3 (a) in Fourier space. One halo pattern, which has a constant radius in all directions, appears as a circle with thick line. The radius of the circle indicates the periodic distance between the Zn band shapes shown in Fig. 3 (a). The central region of the halo pattern appears dark and the border of the circle appears hazy. This is because the distance between the Zn band shapes does not have a constant value, but rather fluctuates. The mean distance between neighbouring Zn band shapes in Fig. 3 (a), which can be calculated from the power spectrum in Fig. 5, is estimated as 0.57 μm . According to the free energy model [16], when the cathode potential was applied to the electric double layer, the separated distributions of Zn^{2+} and Sn^{2+} were formed in the solution near it. Hence, Zn and Sn atoms on the cathode were not required to diffuse to each other and formed their band shapes when Zn^{2+} and Sn^{2+} ions atomised.

3.3 Schematic diagram of the Zn content dependent on V_c

A schematic diagram of the Zn content of Sn–Zn thin films is illustrated in Fig. 6 according to a phenomenological theory of electrodeposition [14-15] when $V_{b\text{Zn}^{2+}} > V_{b\text{Sn}^{2+}}$ where $V_{b\text{Zn}^{2+}}$ and $V_{b\text{Sn}^{2+}}$ are the potential barriers of Zn^{2+} and Sn^{2+} , respectively.

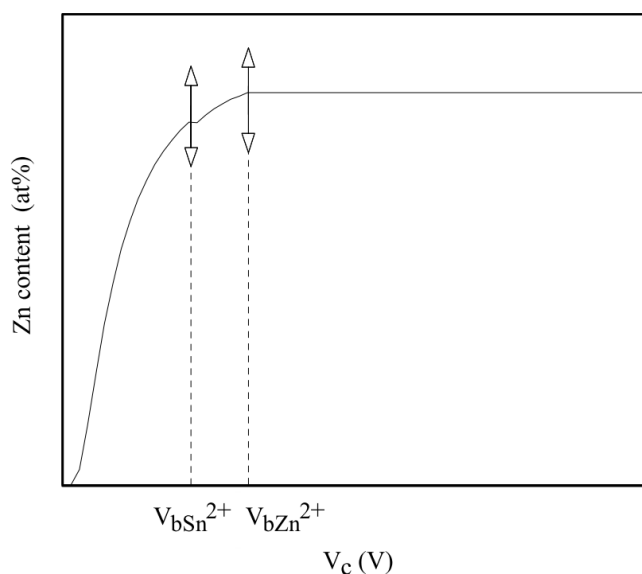


Figure 6. Schematic diagram of the Zn content of Sn–Zn thin films based on the phenomenological theory of electrodeposition.

When V_c is small in Fig. 6, the Zn content remains at 0 at% because the probability of atomisation from Zn^{2+} to Zn is very small. When $V_c < V_{bSn^{2+}}$, the Zn content increases with V_c . At $V_c = V_{bSn^{2+}}$, the Zn content significantly changes at the resonant frequencies of Sn^{2+} , as indicated by the arrows in Fig. 6. With an increase in $V_c \geq V_{bSn^{2+}}$, the Sn mass electrodeposited on Sn–Zn thin films becomes constant and a discontinuity of the slope of the Zn content curve occurs around $V_{bSn^{2+}}$, as shown in Fig. 6. When $V_{bSn^{2+}} < V_c < V_{bZn^{2+}}$, the Zn content increases with V_c . When $V_c = V_{bZn^{2+}}$, the Zn content oscillates significantly at the resonant frequencies of Zn^{2+} . For $V_c > V_{bZn^{2+}}$, the Zn content tends to become constant because the Sn and Zn masses electrodeposited on the Sn–Zn thin films become constant.

There are regions where the Zn contents at $R=1$ and 1.5 in Fig. 2 remain at 0 at% as shown in Fig. 6. When $R=1$ and 1.5 in Fig. 2, the decreases in the Zn content at $V_c = 0.86$ and 0.9 V correspond to the change in the Zn content at resonant frequencies of Sn^{2+} , which are indicated by the arrows in Fig. 6. Hence, the dependence of the Zn content at $R=1$ and 1.5 in Fig. 2 on V_c is consistent with that in Fig. 6.

3.4 Determination of $V_{bSn^{2+}}$ and $V_{bZn^{2+}}$

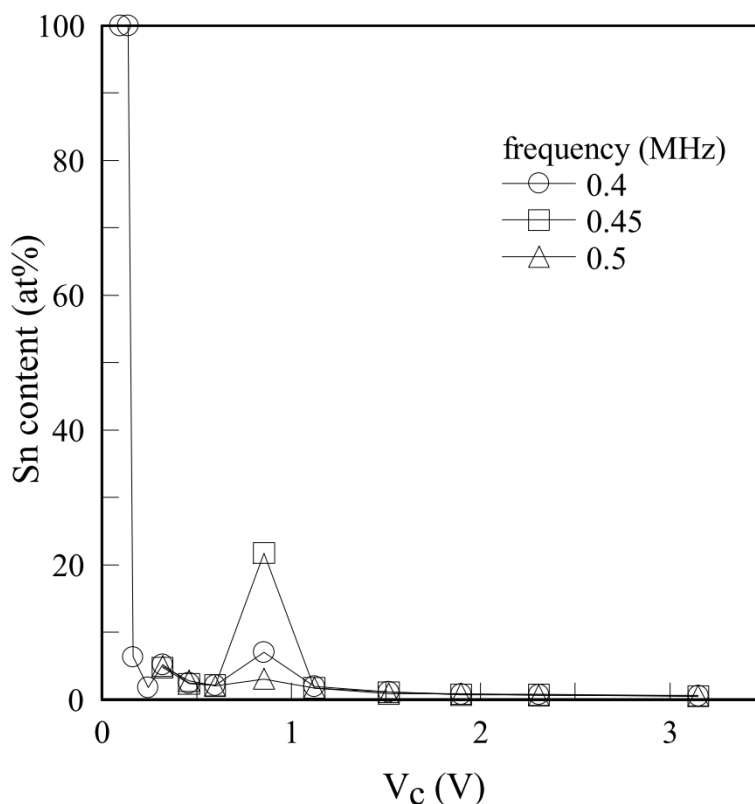


Figure 7. Dependence of Sn content on V_c . The Sn–Zn thin films were electrodeposited from a solution of $R = 1$ at frequencies of 0.4, 0.45, and 0.5 MHz.

Figure 7 shows the dependence of the Sn content of Sn–Zn thin films at $R = 1$ on V_c at 0.4, 0.45, and 0.5 MHz. The Sn content at $V_c = 0.86$ V significantly changes with the frequencies. Hence, $V_{bSn^{2+}}$

is determined to be 0.86 V, which is close to 0.9 V at 0.4 MHz when $R=1.5$. The mean Sn content at $V_c \geq 1.12$ V in the range of 0.4–0.5 MHz is 0.97 at%, which indicates that the Zn content is nearly equal to 100 at %. This is because the oscillation of the Zn content with the frequencies at $V_c \geq 1.12$ V does not obviously appear even if $V_c = V_{bZn^{2+}}$. However, as the Zn content in Fig. 2 tends to become constant at $V_c \geq 1.12$ V, $V_{bZn^{2+}}$ is determined to be 1.12 V.

3.5 Crystalline structure of Sn–Zn thin films

Figure 8 shows XRD charts of Sn–Zn thin films electrodeposited (a) at $V_c = 0.32$ V and 0.4 MHz, and (b) at $V_c = 3.15$ V and 0.4 MHz. The Zn contents of the Sn–Zn thin films at $V_c = 0.32$ and 3.15 V were 94.8 and 99.5 at %, respectively. The diffraction peaks from the Sn–Zn thin films indicate that the Sn–Zn thin films comprise the tetragonal crystal structure β -Sn and HCP crystal structure Zn phase. According to the Sn–Zn phase diagram [8], Sn–Zn alloys comprise the tetragonal crystal structure β -Sn and HCP crystal structure Zn phase in the range of 0.4–99.964 at% Zn at room temperature.

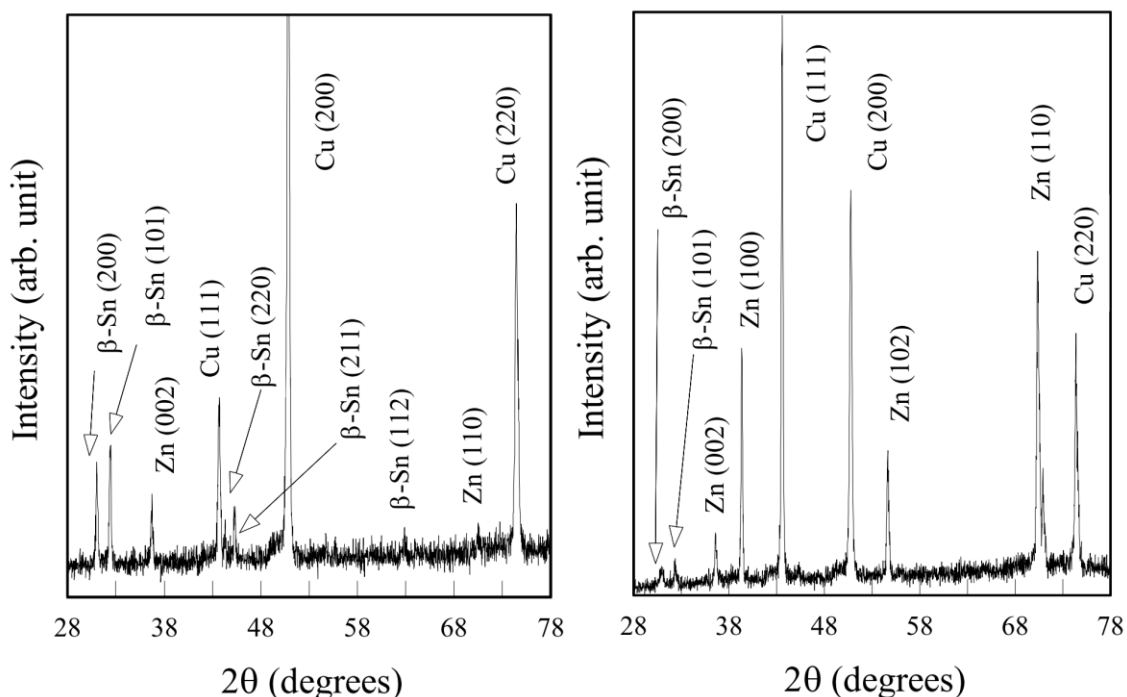


Figure 8. XRD charts of the Sn–Zn thin films formed from a solution of $R = 1$ and at 0.4 MHz: (a) $V_c = 0.32$ V and (b) $V_c = 3.15$ V.

The electrodeposited Sn–Zn thin films have much finer eutectic structures than Sn–Zn alloys formed by the solidification of liquid Sn and Zn [18]. No other phases, such as intermetallic compounds [19], were detected.

4. CONCLUSIONS

Sn–Zn thin films electrodeposited from solutions with $R = 0.18$ – 1.5 with rectangular pulse voltages over a megahertz frequency range were investigated using SEM-EDX and XRD. The phases of the Sn–Zn thin films were divided into two groups according to R : When $R < 1$, the electrodeposits comprised only the tetragonal crystal structure of the β -Sn phase. When $R \geq 1$, the electrodeposits had eutectic structures comprising the tetragonal crystal structure β -Sn and HCP crystal structure Zn. The SEM observations of the eutectic structures revealed that they had a periodic distance of $0.57 \mu\text{m}$ and the Sn–Zn thin films had smooth surfaces formed not by islands, but by layer-by-layer growth. The dependence of the Zn content of the Sn–Zn thin films on the cathode potential was consistent with the phenomenological theory of electrodeposition. The potential barriers of Sn^{2+} and Zn^{2+} were determined to be 0.86 and 1.12 V, respectively.

References

1. A. A. El-Daly, A. E. Hammad, G. S. Al-Ganainy, and A. A. Ibrahiem, *Mater. Des.*, 56 (2014) 594.
2. L. R. Garcia, L. C. Peixoto, W. R. Osório, and A. Garcia, *Mater. Lett.*, 63 (2009) 1314.
3. M. Esfahani, K. S. Munir, C. Wen, J. Zhang, Y. Durandet, J. Wang, and Y. C. Wong, *Surf. Coat. Technol.*, 333 (2018) 71.
4. K. Wang, H. W. Pickering, and K. G. Weil, *Electrochim. Acta*, 46 (2001) 3835.
5. O. S. Fatoba, A. P. I. Popoola, and T. Fedotova, *J. Electrochem. Sci. Technol.*, 6 (2015) 65.
6. O. A. Ashiru and J. Shirokoff, *Appl. Surf. Sci.*, 103 (1996) 159.
7. St. Vitkova, V. Ivanova, and G. Raichevsky, *Sur. Coat. Technol.*, 82 (1996) 226.
8. Z. Moser, J. Dutkiewicz, W. Gasior, and J. Salawa, *Bulletin of Alloy Phase Diagrams*, 6 (1985) 330.
9. G. E. Lloyd, *Mineral. Mag.*, 51 (1987) 3.
10. A. P. Abbott, G. Capper, K. J. McKenzie, and K. S. Ryder, *J. Electroanal. Chem.*, 599 (2007) 288.
11. K.-L. Lin and L.-M. Sun, *J. Mater. Res.*, 18 (2003) 2203.
12. Y. Salhi, S. Cherrouf, M. Cherkaoui, and K. Abdelouahdi, *Appl. Surf. Sci.*, 367 (2016) 64.
13. M. Arici, H. Nazir, and M. L. Aksu, *J. Alloys Compd.*, 509 (2011) 1534.
14. M. Saitou, *Int. J. Electrochem. Sci.*, 15 (2020) 6561.
15. M. Saitou, *Int. J. Electrochem. Sci.*, 15 (2020) 9940.
16. M. Saitou, *Int. J. Electrochem. Sci.*, 14 (2019) 1107.
17. M. Plapp, S. B-Rousseau, G. Faivre, and S. Akamatsu, *Comptes Rendus Mécanique*, 345 (2017) 56.
18. L. R. Garcia, W R. Osório, L. C. Peixoto, and A. Garcia, *Mater. Charact.*, 6 (2010) 212.
19. Z. Hou, T. Niu, X. Zha, Y. Liu, and T. Yang, *J. Mater. Sci.: Mater. Electron*, 30 (2019) 20276.